Journal of Controlled Release 358 (2023) 626–635

Contents lists available at ScienceDirect

Journal of Controlled Release

journal homepage: www.elsevier.com/locate/jconrel

Investigating structural attributes of drug encapsulated microspheres with quantitative X-ray imaging

Andrew G. Clark [a], Ruifeng Wang [b], Josh Lomeo [a], Yan Wang [c], Aiden Zhu [a], Mike Shen [a], Quanying Bao [b], Diane J. Burgess [b], Bin Qin [c], Shawn Zhang [a,*]

[a] DigiM Solution LLC, 500 West Cummings Park, Suite 3650, Woburn, MA 01801, USA
[b] Department of Pharmaceutical Sciences, University of Connecticut, 69 N Eagleville Road U3092, Storrs, CT 06269, USA
[c] Division of Research and Standards, Office of Generic Drugs, Center for Drug Evaluation and Research, FDA, MD, USA

ARTICLE INFO

Keywords:
PLGA microspheres
Manufacturing development
Structural uniformity
Microstructure sameness
X-ray microscopy
AI image analytics

ABSTRACT

The intra-sphere and inter-sphere structural attributes of controlled release microsphere drug products can greatly impact their release profile and clinical performance. In developing a robust and efficient method to characterize the structure of microsphere drug products, this paper proposes X-ray microscopy (XRM) combined with artificial intelligence (AI)-based image analytics. Eight minocycline loaded poly(lactic-*co*-glycolic acid) (PLGA) microsphere batches were produced with controlled variations in manufacturing parameters, leading to differences in their underlying microstructures and their final release performances. A representative number of microspheres samples from each batch were imaged using high resolution, non-invasive XRM. Reconstructed images and AI-assisted segmentation were used to determine the size distribution, XRM signal intensity, and intensity variation of thousands of microspheres per sample. The signal intensity within the eight batches was nearly constant over the range of microsphere diameters, indicating high structural similarity of spheres within the same batch. Observed differences in the variation of signal intensity between different batches suggests inter-batch non-uniformity arising from differences in the underlying microstructures associated with different manufacturing parameters. These intensity variations were correlated with the structures observed from higher resolution focused ion beam scanning electron microscopy (FIB-SEM) and the *in vitro* release performance for the batches. The potential for this method for rapid at-line and offline product quality assessment, quality control, and quality assurance is discussed.

1. Introduction

Poly(lactic-*co*-glycolic acid) (PLGA) is a popular polymer for controlled release (CR) drug products due to its biocompatibility and biodegradability [1–5]. Over the past 30 years there have been >20 PLGA-based CR products approved for use by the FDA in the US. Over half of the aforementioned PLGA products are CR microspheres, where the drug is dispersed in a polymer matrix formulated as spherical particles [6]. PLGA microspheres are a well-known platform for CR products owing to their ability to encapsulate a wide range of drugs (including small molecules and peptides), easy local administration (*e.g.*, using a syringe), as well as sustained release for long periods of time [7]. Despite the advantages of the PLGA microsphere platform, there is a scarcity of PLGA microsphere drug products on the market. The difficulty in reliably relating the structural critical quality attributes (CQAs) to formulation, process conditions, and performance presents a significant barrier to the development of new and generic PLGA microsphere products [6–10].

Recognizing the critical role that microstructures can play in the performance of complex drug products (*e.g.*, topical dermatologic products), the FDA has recommended comparative characterization of microstructure (Q3) studies as part of bioequivalence assessment when applicable, *i.e.*, the demonstration of "a similar arrangement of matter" between a proposed generic product and the reference listed drug (RLD) [11]. In the case of PLGA microspheres, a major factor governing drug release and performance is the underlying structure of the formulation, including the microsphere size distribution, distribution of active pharmaceutical ingredient (API) within the spheres, and the presence of any porosity [12,13]. Accordingly, characterization of the microstructure of these microspheres can serve as a quantitative pathway toward

* Corresponding author.
E-mail address: shawn.zhang@digimsolution.com (S. Zhang).

https://doi.org/10.1016/j.jconrel.2023.05.019
Received 15 February 2023; Received in revised form 3 May 2023; Accepted 14 May 2023
Available online 22 May 2023

establishing Q3 bioequivalence.

Traditional bulk techniques such as laser diffraction, porosimetry, and particle imaging, can be used to rapidly determine microstructure characteristics such as microsphere size distribution and surface features. Figs. 1a-b show example scanning electron microscopy (SEM) images of microspheres where the size distribution and surface features can be readily observed. However, these techniques are surface limited, and unable to directly measure and quantify the underlying distribution of API, porosity, or excipients within the microspheres. Imaging of microsphere products allows for a direct visualization of the microsphere's microstructure in its final product form. From these images the drug loading, spatial distribution as well as porosity distribution are directly quantified. With these characteristics, a true mechanistic understanding of product performance can be obtained. For instance, a microsphere might have an internal polymer barrier between the loaded API and the surface of the sphere, which may result in a slower release rate. Direct visualization *via* microstructure imaging allows for explicit characterization of this inherently structural feature, which is nearly impossible to characterize by current surface methods.

High resolution electron imaging combined with ion milling, *i.e.*, focused ion beam (FIB) SEM, and AI image analytics have been shown to be powerful tools for directly quantifying the intra-sphere microstructure of PLGA microsphere samples [12,14]. Fig. 1c shows a representative image of a microsphere cross-section obtained using FIB-SEM, while Fig. 1d shows the AI assisted 3D reconstruction of hundreds of FIB-SEM images of the microspheres. Despite the powerful elucidation and quantification of intra-sphere microstructures, FIB-SEM is limited by its throughput as the technique requires several hours of imaging and analysis to determine the microstructure of one microsphere [12,13,15]. The time and cost required to determine the microstructure of a statistically representative number of microspheres would be prohibitive. A complimentary approach is needed to determine the overall microsphere structural uniformity efficiently. X-ray microscopy (XRM) is an imaging technique that has recently gained attention for its ability to non-invasively characterize the microstructure of pharmaceutical samples. XRM is a technology in the family of X-ray micro-computed tomography (microCT) and operates under the same principle as medical CT scans, with 3 orders of magnitude of resolution improvement. XRM has recently been demonstrated as a powerful tool in quantifying the microstructure of long-acting implants, oral solid tablets, and a variety of spray dried intermediates, granules, and raw compound powders [16–19]. Compared to FIB-SEM's one particle characterization at a time, XRM is capable of imaging hundreds to thousands of micron sized spray dried particles in less than half the amount of time needed to conduct a full 3D FIB-SEM image collection for a single particle [16].

In this work, XRM was utilized to characterize the structures of eight batches of PLGA microsphere samples manufactured under different process parameters. All polymer properties (*e.g.* molecular weight, L:G ratio, *etc.*) and drug properties were kept the same among the eight microsphere batches, thus ensuring that the only differences among the spheres would be due to the processing conditions of each sample. These processing condition changes will promote variations in the internal structure such as relative fractions of each phase, phase size and spatial distributions which have been shown to impact *in vitro* release performance [12,14,15,17]. XRM was utilized here to characterize the impact of these structural changes through AI-based analysis of the signal intensity of the microspheres. Through high resolution XRM and AI analytics, the XRM signal intensity and intensity variation of the microsphere samples were measured for thousands of microspheres per batch to achieve a statistically representative sampling. The intensity and intensity variation were assessed to determine similarity in microstructures of microspheres intra-batch and inter-batch. The average intensity variation for the batches was correlated to their *in vitro* release profiles to connect the microstructure properties to the final product performance. Four of these samples have been previously investigated using FIB-SEM and AI-image analytics to quantify their underlying microstructure attributes and relate those to their process parameters [14]. By correlating the previous FIB-SEM microstructure characterizations to this XRM investigation, a correlative workflow was proposed that synergizes rapid assessment of many microspheres using XRM with detailed characterization using FIB-SEM. Use of this correlative imaging approach to quantitatively compare the Q3 attributes of microspheres, *e.g.*, from different batches or different manufactures, will be discussed.

2. Materials and methods

2.1. Materials

PLGA (Resomer® RG503H) was a gift from Boehringer-Ingelheim. Micronized minocycline hydrochloride was generously provided by

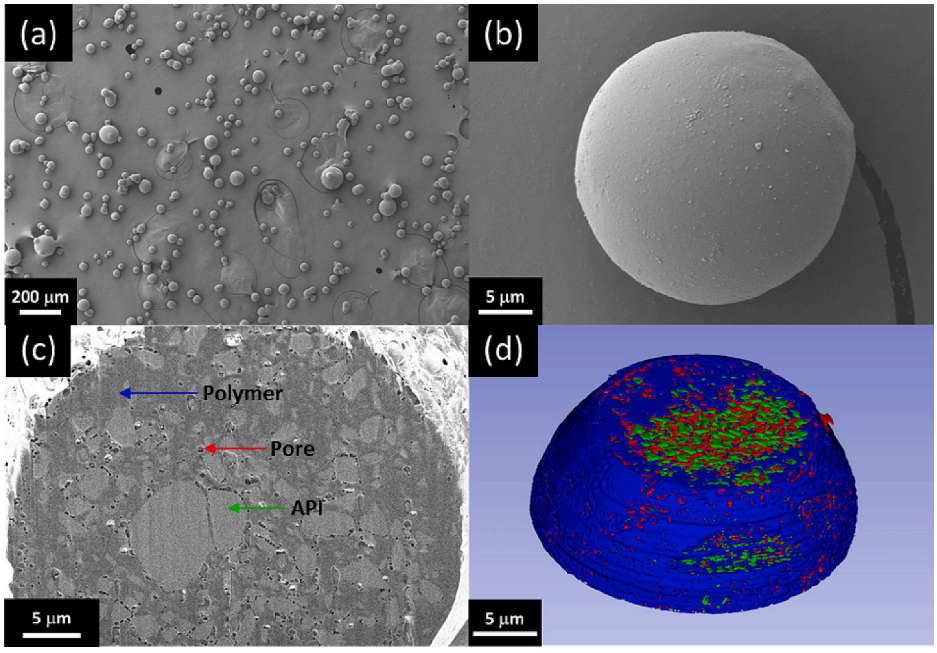

Fig. 1. (a) Controlled release PLGA microspheres as viewed by SEM. (b) Individual microsphere sample. (c) Cross-sectional view of a microsphere after focused ion beam (FIB) milling showing the polymer phase, API phase, and porosity as indicated. (d) Reconstructed 3D model of a FIB milled microsphere with the polymer phase (blue), API phase (green), and porosity (red). (For interpretation of the references to colour in this figure legend, the reader is referred to the web version of this article.)

Hovione (Loures, Portugal). HPLC-grade dichloromethane (DCM), and ethyl acetate (EA) and hexane were purchased from Fisher Scientific (Pittsburgh, PA, USA). Silicone oil (350 cSt and 1000 cSt), poly (vinyl alcohol) (PVA, Mw: 30–70 kDa), and phosphate-buffered saline (PBS) were purchased from Sigma-Aldrich (St. Louis, MO, USA). Milli-Q® water was used for the preparation of *in vitro* release testing media. All other chemicals were purchased as analytical-grade reagents.

2.2. Preparation of minocycline hydrochloride microspheres

PLGA with molecular weight similar to the commercial product Arestin® was used to prepare compositionally equivalent minocycline hydrochloride microspheres using the coacervation method [14,20]. The process conditions of the eight microsphere formulations are listed in Table 1. Briefly, PLGA was dissolved in either DCM or EA, then the micronized minocycline hydrochloride powder was suspended in PLGA solution, followed by transferring into a vessel equipped with an overhead stirrer. Silicone oil was added to the solution while stirring to induce coacervation. The dispersed coacervate was subsequently discharged into hexane for solidification. Following solidification, the microspheres were washed and dried *in vacuo* prior to final collection. All the prepared microspheres showed similar drug loading and can be considered compositionally equivalent.

2.3. Particle size distribution

The particle size distribution of the prepared microsphere formulations was tested using an AccuSizer autodiluter particle sizing system (Nicomp, Santa Barbara, CA, USA) under light extinction mode. Briefly, approximately 8 mg of microspheres were dispersed in 0.6 mL of 1% (*w/v*) PVA solution. 100 μL of the dispersion was then injected into the system for particle size analysis.

2.4. In vitro release testing of prepared minocycline microspheres

The *in vitro* release testing of the prepared minocycline hydrochloride microspheres was conducted using a previously developed sample-and-separate method [21]. Briefly, approximately 4 mg of microspheres were dispersed in PBS (10 mM, pH 7.4) containing 0.02% (*v*/v) Tween 20 at 37 °C. At predetermined time intervals, the release media was tested *via* HPLC to determine the cumulative drug release. All *in vitro* release tests were conducted in triplicate and the results were reported as mean % cumulative release ± standard deviation.

2.5. X-ray microscopy (XRM)

A Zeiss Xradia Versa 520 X-ray microscope (Carl Zeiss Microscopy, USA) was used to obtain the sample images. A schematic of the image acquisition is shown in Fig. 2a. The microsphere samples were loaded into a plastic tube as a powder bed, and mounted vertically on a rotating sample stage between the X-ray source and the X-ray detector. To avoid imaging artifacts arising from the sample container, the X-ray source was focused to only the interior volume of the sample holder that contained the microspheres. An initial X-ray radiograph was taken at the beginning of the scan using an exposure of 0.5 s and an X-ray source energy of 80 keV.

Table 1
PLGA microsphere samples and preparation conditions.

Sample ID	Solvent	Stirring speed (RPM)	Silicone oil η (cSt)
FA	DCM	350	350
FB	DCM	350	1000
FC	DCM	600	350
FD	DCM	600	1000
FE	EA	350	350
FF	EA	350	1000
FG	EA	600	350
FH	EA	600	1000

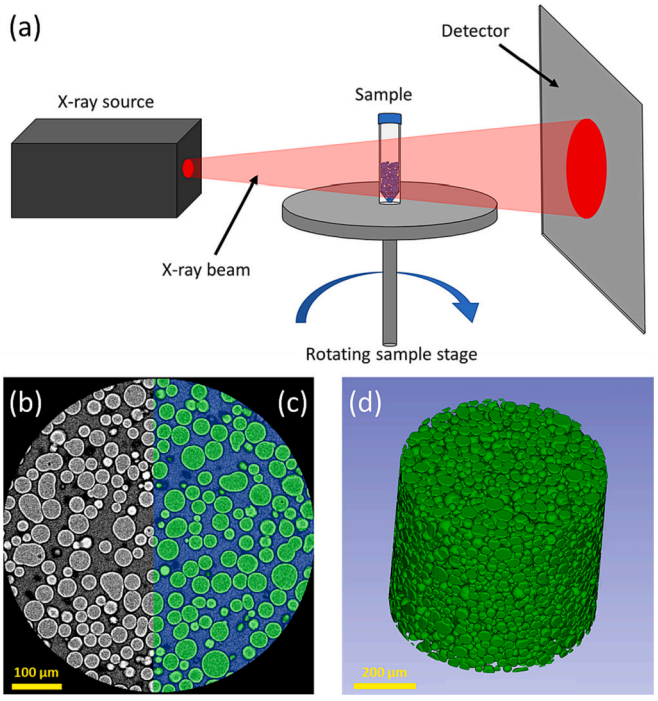

Fig. 2. (a) Cartoon schematic demonstrating the principal of operation of XRM. (b) 2D slice of a reconstructed XRM image of a microsphere sample with (c) an example segmentation of the microspheres (green) from the surrounding air (blue). (d) 3D rendering of the imaged XRM volume showing all segmented microspheres. (For interpretation of the references to colour in this figure legend, the reader is referred to the web version of this article.)

Following this initial exposure, the sample container was rotated by 0.09 degrees before acquiring another radiograph at the same exposure time and X-ray source energy. This procedure was iterated to obtain 4000 radiographs. Scanned radiographs were reconstructed into 3D cross sectional images with 1000x1000x1000 voxels using a filtered backward projection algorithm with a bin averaging value of 2, resulting in an effective voxel size of 0.5 μm. Fig. 2b shows a representative 2D cross section of the scan. All imaging and subsequent analysis were conducted in 3D.

2.6. Image analytics

Image analytics were performed using DigiM™ I2S cloud-based image analysis platform (DigiM Solution, USA). The 3D XRM images were subjected to an initial intensity normalization procedure using the sample container and the inter-sphere air as the calibration standards. Following the image intensity normalization, the images were segmented into either the microsphere phase or inter-sphere air phase using iterative supervised machine learning and deep learning methods [22–24]. In brief, a small crop of a 2D cross sections of the XRM scan from one sample was used to train a supervised machine learning model based on the Random Forest classification algorithm. Once the training is considered satisfactory, it is applied to 5 arbitrarily selected cross section images from the XRM scans of each sample. The segmentation of 40 cross section images from 8 samples was used as a training dataset to train a neural network deep learning model, which was then used to segment the 3D images of all 8 formulations. An example of the AI segmentation for a single 2D image (Fig. 2b) is shown in Fig. 2c, and the full 3D rendering of the segmented microspheres in the entire imaged volume is shown in Fig. 2d. From this initial segmentation, the microsphere size distribution is obtained. During X-ray imaging, X-ray

photons will diffract on the structures of the imaged object, resulting in constructive interference of the X-ray wavefronts which produces a significant brightening of the edge of the imaged object [25]. To mitigate the impact of diffraction enhanced edge intensity on subsequent analysis of the microsphere intensities, the segmentations of microspheres were eroded by five pixels from their peripheral edges. Following this correction, the average greyscale intensity and standard deviation of intensity for every imaged microsphere was measured.

3. Results and discussion

3.1. Particle size distribution characterization

2D cross-sectional images of the XRM scans for the eight microsphere samples are shown in Fig. 3a-h. All eight samples have similar sphere morphologies, displaying both individual microspheres as well as occasional fused particles. Porosity is visible in the XRM images; however, no large void spaces nor cavities were observed, confirming good encapsulation coherency of the drug within the microspheres.

Following AI segmentation of the microspheres from the inter-sphere air, the microsphere particle size distributions (PSD) were determined and are shown in Figs. 4a-b. The PSDs shown in Figs. 4a-b represent the cumulative volume distributions as determined from the XRM images. The volume distribution was used as opposed to the number distribution due to the method of measurement from the images. After the AI segmentation, the individual microspheres are determined by using watershed algorithms which then determine the number of voxels that make up a given microsphere. Combined with the knowledge of the voxel resolution, this returns the volume of each sphere, and the subsequent equivalent spherical diameter. From these data, calculation of the volume distribution is straightforward. Samples formulated in DCM (FA-FD) show very similar distributions (Fig. 4a), with sample FC showing the largest size spheres of these four batches. For samples formulated in EA (FE-FH) (Fig. 4b), the distributions show a greater range compared to the previous four samples. The particle size distribution was also independently measured using an AccuSizer system under the light extinction mode. The D10, D50, and D90 values determined from XRM were plotted as a function of the corresponding AccuSizer measurements (Fig. 4c).

XRM particle size measurements can allow rapid and accurate in-line quality control tests for microsphere formulations. XRM-based PSD is a complimentary, and possibly improved, means of measuring sphere sizes compared to the AccuSizer light extinction method. While the D10 values are fairly comparable, the D50 and D90 from the XRM measurements are significantly smaller than the values determined using the AccuSizer as seen by the deviation of the data points from the one-to-one line in Fig. 4c. For accurate measurements of particle size using laser diffraction, lihgt extinction, or light obscuration, it is crucial to ensure the particles are well dispersed during measurement [26]. If the particles aggregate, the measurement will overestimate the true particle size distribution by reporting these aggregates as large individual particles. XRM combined with AI-analytics does not require that the microspheres be well dispersed as the AI segmentation can recognize individual spheres within particle aggregates. Furthermore, XRM is a non-invasive technique and can image the microspheres as is, whereas for AccuSizer measurements, the spheres must be dispersed in suitable media often involving use of either surfactants or sonication, both of which may affect the PSD measurement.

The PSDs of microsphere formulations as a function of their solvents as well as coacervation process parameters offers deeper insight into the impact of manufacturing parameters on final product characteristics. Interestingly, regardless of solvent used, the microspheres prepared using the silicone oil with lower viscosity were larger as shown in Fig. 4. This is true for both the AccuSizer and the XRM measurements, indicating that the viscosity of silicone oil is a critical process parameter that controls particle size. Samples FD and FH are consistently the smallest microspheres for the DCM and EA samples respectively, indicating that the higher stirring speed and silicone viscosity produce smaller microspheres regardless of the solvent used. The inter-play between process parameters, microsphere microstructure, and release performance are subjects of an on-going modeling investigation. For the XRM measured PSD, the rank order of the D50 is FA > FC > FB > FD and FE > FG > FF > FH for the DCM microspheres and EA microspheres, respectively. In the case of the AccuSizer measurements, these rank orders are slightly different with FC > FA > FB > FD and FG > FE > FF > FH. This switch in rank ordering between XRM determined PSD and AccuSizer determined PSD may result from a greater tendency of samples FC and FG to form aggregates, for which the AccuSizer is more biased to identify particle aggregates as individual particles.

3.2. Intra-batch microstructure characterization

In transmissive X-ray imaging, X-rays pass through an object and are recorded at the detector which measures the total X-ray photon count. The more X-ray photons that arrive at the detector, the greater the signal intensity and the brighter the subsequent reconstructed image will be. As the photons pass through the material, they interact with the atoms present within the sample, and will be attenuated or absorbed

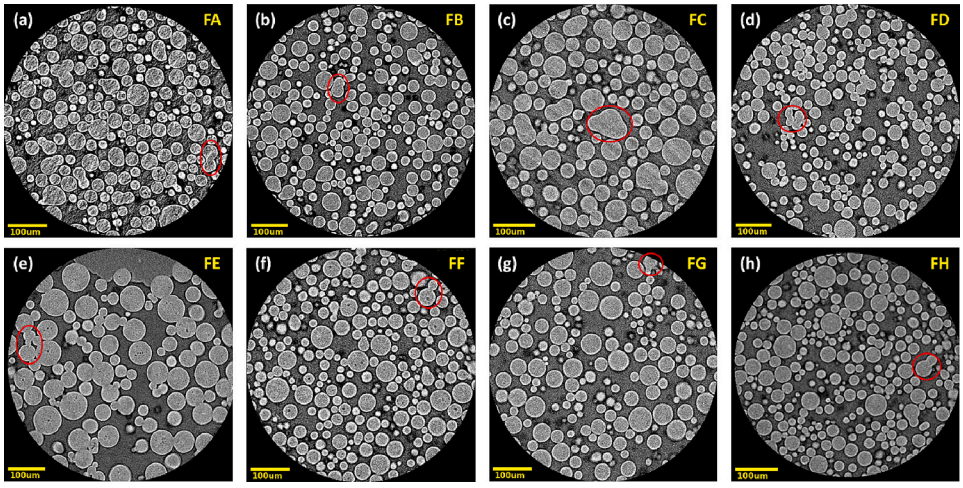

Fig. 3. Cross sectional XRM images of the eight different microsphere samples corresponding to Table 1, with examples of fused microsphere particles circled in red. (For interpretation of the references to colour in this figure legend, the reader is referred to the web version of this article.)

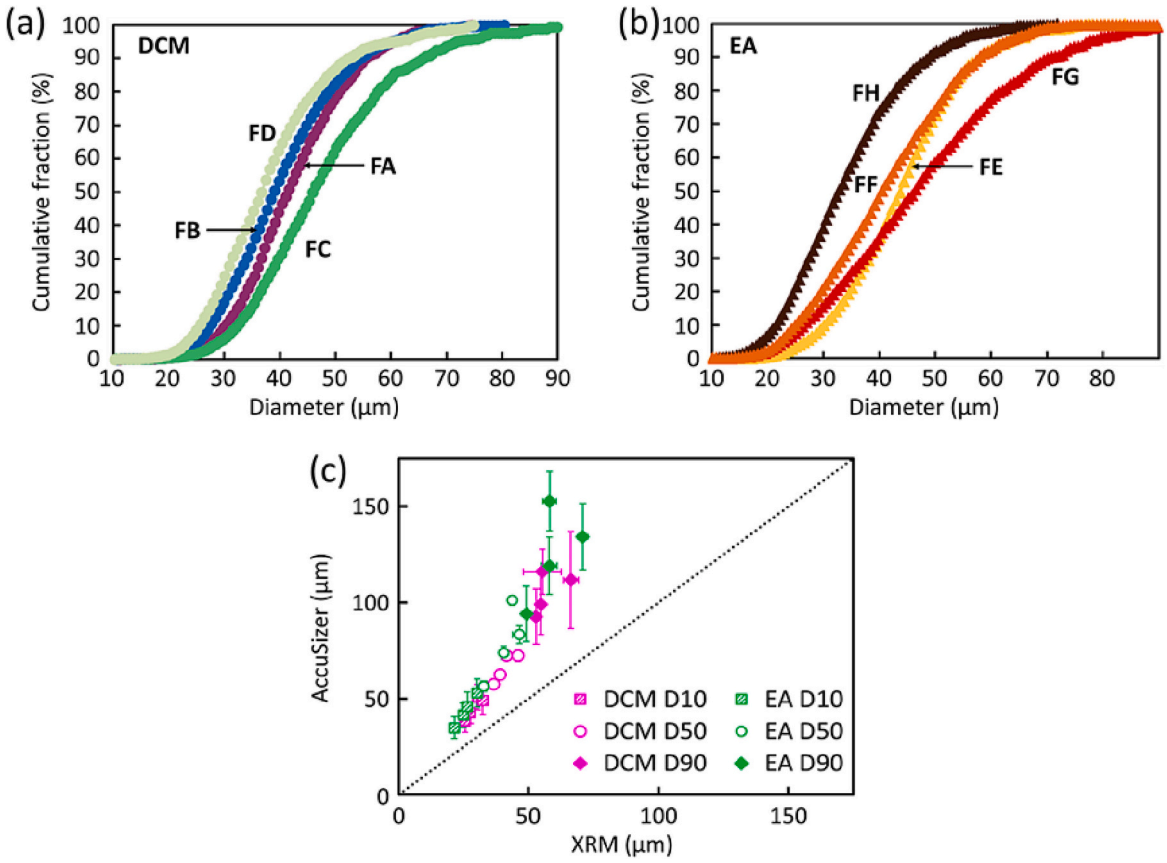

Fig. 4. Particle size distributions quantified from XRM for (a) dichloromethane (DCM) samples FA-FD, and (b) ethyl acetate (EA) samples FE-FH. (c) Plot of the D10 (shaded squares), D50 (open circles), and D90 (filled diamonds) measured by XRM as a function of the AccuSizer measurements, with the dotted line corresponding to the one-to-one agreement between the two measurements. Microspheres prepared in DCM are marked in magenta, and those prepared in EA are marked in green. (For interpretation of the references to colour in this figure legend, the reader is referred to the web version of this article.)

depending on the incoming photon energy and the specific atomic species that the X-ray interacts with [27,28]. The measured X-ray signal intensity will therefore depend on the specific elemental composition of the material as well as how many absorbing atoms are in the photon's path (*i.e.*, the material's density). If the elemental composition is identical between two samples, then variations in the X-ray signal intensity will arise primarily from spatial variations in the density of the two samples. In the particular XRM system used in this study, denser materials are brighter in the reconstructed image. For microspheres within the same batch, the elemental composition will be identical. Any variations in XRM signal intensity will therefore arise from variations in either the porosity of the microspheres or the amount of drug encapsulated.

For the microsphere samples studied, the intensity of the image signal of each observed microsphere is measured following AI-segmentation. Fig. 5a shows the measured signal intensity for all eight microsphere samples with the curves vertically shifted for clarity. For all eight samples, the intensity varies strongly for small microspheres below 10 μm and then levels off for the larger microspheres. The variation of intensity at small diameters arises for two reasons. When the microspheres are small, one drug particle, or one large pore, can significantly alter its average intensity. Additionally, smaller microspheres are further influenced by the image resolution. At 0.5-μm resolution, the intensity of these small spheres is subject to lower signal-to-noise ratio (SNR). As the diameter of the observed spheres increase, the SNR increases proportionally to the total number of voxels of the imaged sphere. Above 20 μm in diameter, the microsphere signal intensity shows little to no variation. This indicates that the spheres >20 μm within a batch have the same X-ray signal intensity, due to similarity in both drug loading and porosity/void fraction, confirming excellent intra-batch structural uniformity. Furthermore, the total number of imaged microspheres (indicated parenthetically in Fig. 5a) is in the thousands, signifying the statistical representativeness of this measurement.

While the measurement of the X-ray signal intensity can inform on the similarity in the microstructure of microspheres intra-batch, it is limited by the inability to compare the value of the signal intensities between batches. The overall distribution of pixel intensities of the samples will have the same shape due to the same material composition. However, slight variations in sample preparation and imaging conditions, such as the packing density in the microsphere powder bed, will result in slightly different histogram distributions, which prevents a direct sample-to-sample comparison of different batches. For a more direct, quantitative comparison, multiple intensity calibrants need to be employed to properly match the intensity histograms. Ideally this would be achieved *via* reference standard materials that can be co-imaged with the microsphere samples and provide scan-to-scan intensity calibration. Furthermore, if these standards had well-known densities, then the X-ray intensity signal could be converted into a density measurement, allowing for determination of the individual microsphere density and phase identification. This quantitative density characterization method with a systematic calibration will be reported in a follow-up publication [29]. The new method will include a diffraction artifact correction improved from the more empirical five-pixel erosion approach used in this study.

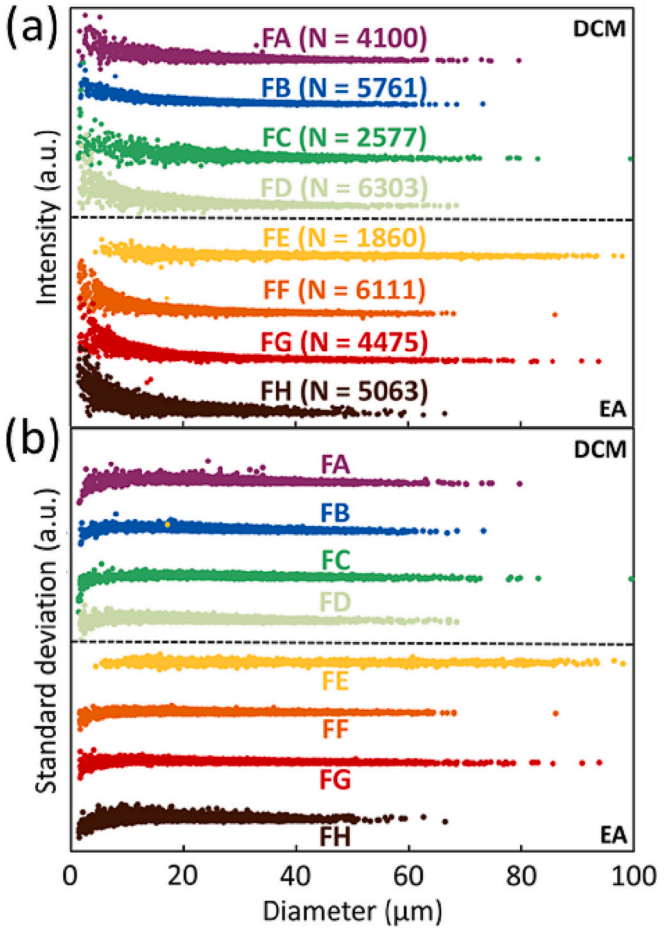

Fig. 5. (a) Average XRM intensity as a function of microsphere diameter for the eight different samples, with the total number of microspheres indicated parenthetically. (b) Standard deviation of the XRM intensity as a function of microsphere diameter for the eight different samples. For both plots, the samples above the dotted line were synthesized in DCM, and below the dotted line synthesized in EA. Curves have been vertically shifted for clarity.

3.3. Inter-batch uniformity

While batch-to-batch variations of microsphere microstructures cannot be assessed from the X-ray signal intensity itself, it can be assessed from the variance of signal intensity per microsphere. The variations of the intensity of a microsphere will not depend on an exact match between the different sample X-ray intensity histograms and can therefore be directly compared. The standard deviation of the XRM signal intensity for a microsphere informs on the variation and distribution of the material phases that comprise the microsphere. If the microsphere has a perfectly even distribution of phases, then every voxel (3D version of an image pixel) will have the same intensity value and the standard deviation will be zero. If the phase distribution is highly non-uniform, then there will be a wide range of voxel intensity values, thus resulting in a large standard deviation. This non-uniformity can arise from variations in the spatial distribution of the material phases which have been demonstrated to be a potential CQA for these microspheres [14].

Fig. 5b shows the measured standard deviation in X-ray signal intensity of each microsphere for all eight samples with the curves vertically shifted for clarity. For all eight batches the standard deviation is nearly constant across all microsphere sizes within a batch, offering further confirmation of the good intra-batch uniformity of the microsphere samples. Fig. 6 shows the average value of the standard deviation for all eight batches compared to each other. FC shows the largest

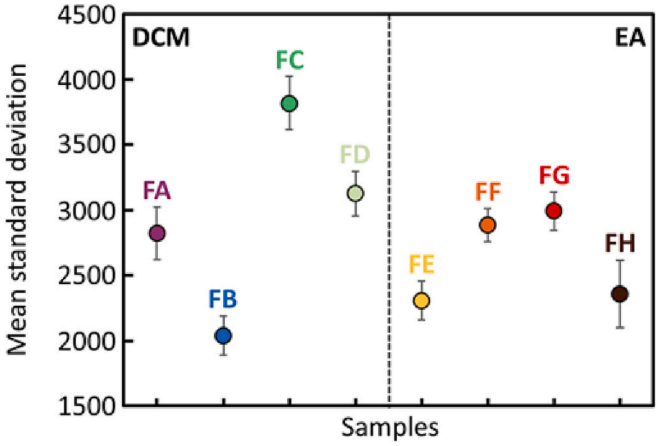

Fig. 6. The mean standard deviation of XRM intensity of all microspheres for the eight samples. Samples prepared using DCM are to the left of the dotted line and those synthesized in EA are to the right.

average standard deviation value among the eight batches while FB shows the smallest average standard deviation.

To better visualize the physical meaning of the standard deviation of the microsphere XRM image signal intensity, the samples with the greatest difference in standard deviation (FB and FC) are shown in Fig. 7a and d, respectively. The microspheres of sample FB seen in Fig. 7a show a uniform signal intensity with little variation in greyscale intensity. A zoomed in view of an example microsphere is shown in Fig. 7b, demonstrating the relatively uniform signal intensity.

In contrast, sample FC shown in Fig. 7d, displays mottled microspheres, with the microspheres showing regions of high X-ray signal (bright spots) and low X-ray signal (dark spots). This signal variation is more clearly seen in the zoomed in view of an example microsphere shown in Fig. 7e. Signal intensity is directly proportional to the underlying density of the region, therefore, a significant variation in signal intensity would mean a non-uniform distribution of phases within the microspheres. To confirm this, Fig. 7c and f show a representative FIB-SEM cross sectional image of a single sphere from samples FB and FC, respectively. The different material phases identified using machine learning are shown, with the polymer phase in blue, API phase in green, and porosity in red. Sample FC shows significantly non-uniform distributions of both API and porosity, whereas sample FB shows API and porosity uniformly dispersed throughout the microsphere. These FIB-SEM images confirm that variations in X-ray signal intensity in a given microsphere are indicative of non-uniformity in the phase distributions within the microspheres. Bright and dark pixel regions in XRM arise from dispersion of primary API particles and pores in drug-rich and drug-scarce domains, respectively. Furthermore, the constant standard deviation across all microsphere sizes indicates the underlying microstructure of the spheres shown in Figs. 7a-b and 7d-e are representative of the overall batch. The result of these analyses suggests that the eight batches have substantial differences in inter-batch microstructure. This observation is consistent with the variations in the process parameters, which were designed to promote microstructure variations between the batches.

3.4. Correlation between XRM signal intensity variation and in vitro release

The standard deviation of the X-ray signal intensity can be treated as a quantitative representation of the difference in the underlying structure of the microspheres. A greater standard deviation implies a greater degree of difference in the distribution of the active ingredient, polymer, and porosity. It has previously been shown that variations in the distribution of the API and pore phases of PLGA microspheres can greatly

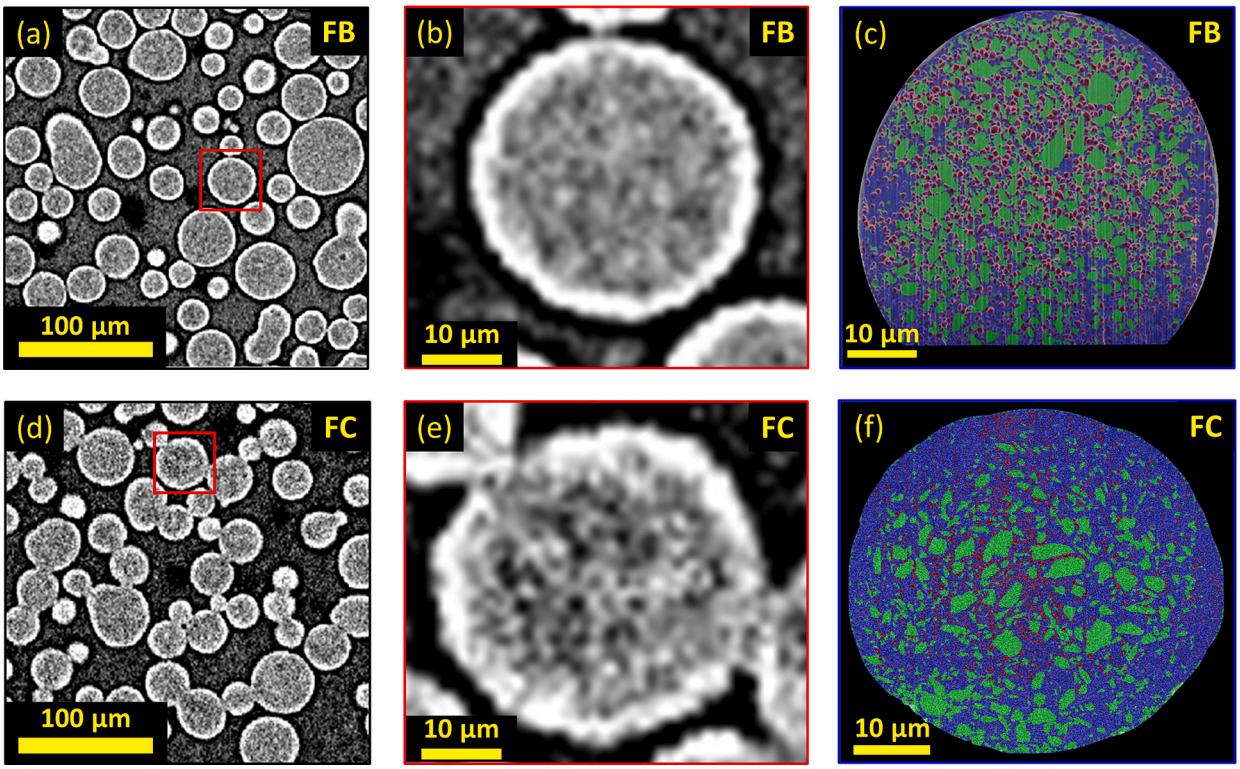

Fig. 7. Example XRM images of (a) sample FB with lowest signal standard deviation and (d) sample FC with the highest signal standard deviation among the microspheres. Zoomed in view of example microspheres for both (b) FB and (e) FC highlighting the relative variations in signal intensity as shown by the variation in the greyscale intensity. FIB-SEM images of: (c) FB and (f) FC with the different segmented material phases shown in colour, demonstrating the uniform material distributions in FB and non-uniform distribution in FC (polymer phase = blue, API = green, pores = red). (For interpretation of the references to colour in this figure legend, the reader is referred to the web version of this article.)

impact their *in vitro* release performance [14]. Correlating the average standard deviation of the X-ray signal to the *in vitro* release performance can allow for rapid assessment of overall batch quality. Fig. 8a and b show the *in vitro* release profiles for the eight samples. All eight formulations show distinctly varied *in vitro* release profiles. In order to verify that these variations arise from the processing conditions and not batch-to-batch variations, the batches were manufactured on different days and their *in vitro* release profiles were compared. An example of this is shown in the Supporting Information (Fig. S1) for formulation FE. The *in vitro* release profiles are identical indicating that the formulation preparation process is stable and repeatable. From the release profiles in Fig. 8a-b, samples FF and FG demonstrate highly similar release profiles with comparable initial release and time to complete release. This would suggest that the standard deviation of the XRM intensity between these two should be nearly identical, and indeed they are very similar as shown in Fig. 6. To obtain a quantitative representation of the *in vitro* release performance, the release profiles are fit at early time points ($t < 1$ day, 5 time points) and late time points ($t > 1$ day, 26 time points) to a Higuchi model [30,31]:

$$\phi(t) = k_H t^{1/2} \quad (1)$$

where $\varphi(t)$ is the fraction of drug released at time t, and k_H is the Higuchi constant. A Higuchi model was chosen for these data as the primary release mechanism was assumed to be diffusion driven [31]. Fits to eq. 1 are shown for both DCM synthesized microspheres and EA synthesized microspheres in Supplementary Figs. S2 and S3 respectively. The Higuchi constant for both early and late times is plotted as a function of the mean standard deviation in Fig. 8c and d. Both early and late time Higuchi rates show good inverse correlation with the mean standard deviation as shown by the dotted lines in Fig. 8c and d. In general, this trend signifies that samples with higher mean standard deviations, thus, greater intra-batch fluctuations in phase distributions from microsphere to microsphere show slower drug release. This holds true for both early and late release epochs, which implies that the phase distribution affects the overall release for these products irrespective of the specific release mechanisms (*e.g.*, diffusion driven, erosion driven, *etc.*). While a majority of the samples show good correlation between XRM standard deviation and their Higuchi release rate constant, there are some notable exceptions. For the early times samples FF and FH show slower Higuchi rates than predicted from the XRM intensity analysis, indicating a slower than anticipated burst release for these samples. At late times, sample FD shows faster Higuchi rate than predicted, indicating faster late-stage release potentially arising from more significant polymer degradation. For both early and late release, sample FD does not agree well with the observed correlation. It is interesting to note that FD and FH were prepared using identical higher viscosity silicone oil (1000 cSt) as well as higher stirring speed (600 rpm). Furthermore, these two samples differ quite significantly in overall release, with FD achieving nearly complete release after 7 days and FH completing release after 14 days. The silicone oil viscosity and stirring speed used for these samples led to strong deviations from the XRM standard deviation prediction. The solvent used in microsphere preparation also impacts the drug release, with the DCM sample showing faster release (sample FD) and the EA sample showing slower release (sample FH).

3.5. FIB-SEM/XRM correlative workflow

The presented analysis using XRM imaging and AI image analytics is a powerful tool that allows for characterization of the intra-batch and inter-batch microstructure to better understand the impact of manufacturing parameters on microstructure, and the impact of microstructure on product performance. While the technique offers immediate insight into the microstructure of a controlled release

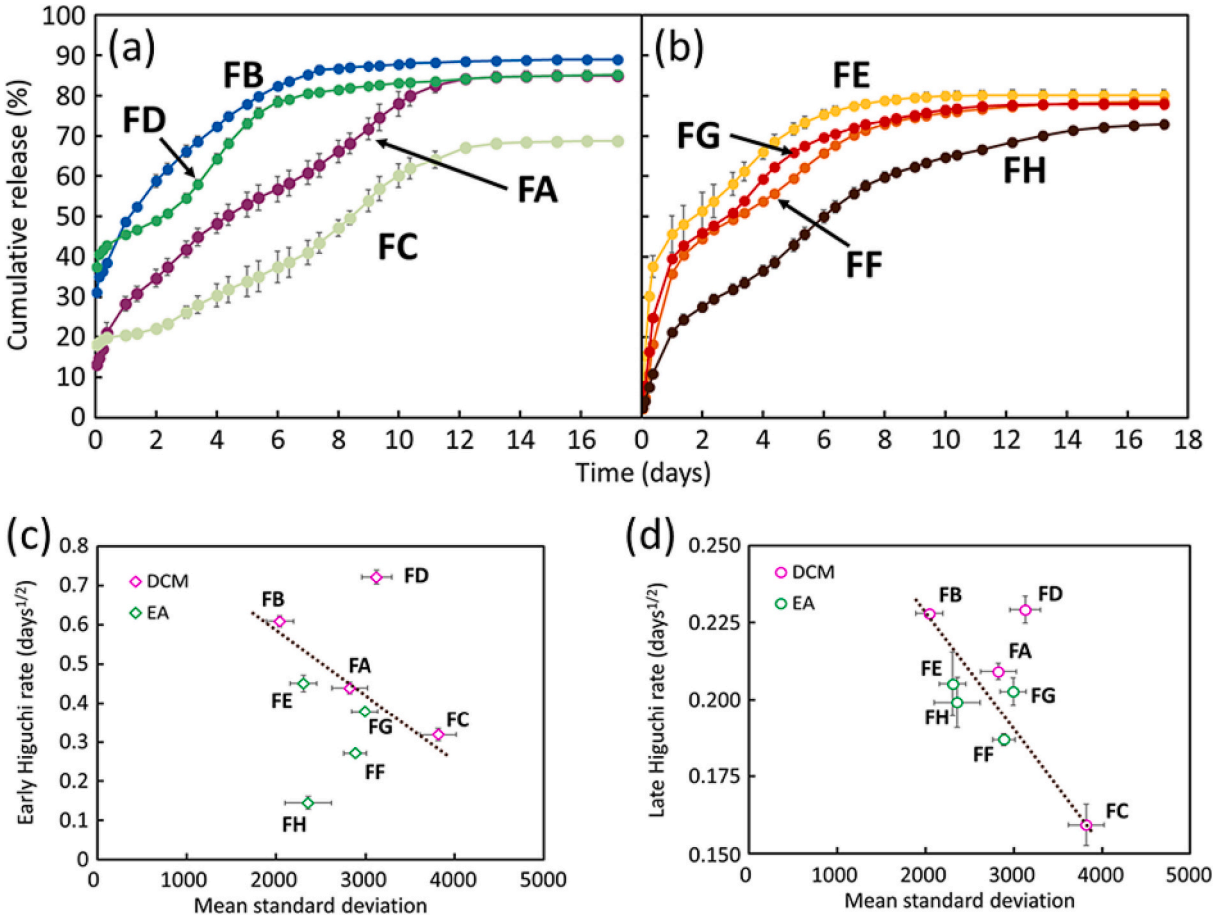

Fig. 8. *In vitro* release profiles for (a) samples FA-FD and (b) samples FE-FH. Higuchi rate determined from the *in vitro* release data plotted as a function of mean standard deviation for (c) early release ($t < 1$ day) and (d) late release ($t > 1$ day), with samples synthesized in DCM marked in magenta and samples synthesized in EA marked in green. (For interpretation of the references to colour in this figure legend, the reader is referred to the web version of this article.)

microsphere product, there are several limitations to the method. At 500 nm resolution, a feature must be 1–2 μm in size to be fully resolved. If the phase features such as API or porosity are below this limit, then XRM will rely on sub-resolution intensity variations which are susceptible to XRM imaging artifacts like beam hardening, while increasing the uncertainty in assessment of the microsphere uniformity. Considering the limitations, it becomes clear that XRM cannot be the only tool to be used in characterizing controlled release microsphere products. The advantage of XRM imaging and characterization of microspheres lies in its ability to interrogate the microstructure of these products directly and non-invasively. In this light it serves as a powerful complimentary approach to the more traditional physico-chemical characterization methods including *in vitro* release testing, thermal analysis, and spectroscopy. Due to its resolution limitations, XRM is not intended to inform on any nanometer scale features, which is the scale of interest for higher resolution imaging like FIB-SEM [14]. XRM, however, is most powerful when characterizing inter- and intra-sphere uniformity at micrometer scale, thus opening up the potential of new suite of CQAs for microsphere development and regulation.

To mitigate the resolution and field of view limitations from any single imaging method, a correlative workflow combining both the XRM inter-sphere analysis as well as in depth FIB-SEM intra-sphere microstructure characterization is proposed as shown in Fig. 9. The microsphere batches were initially imaged using the XRM workflow as shown in left side of Fig. 9. This XRM imaging is followed by AI segmentation of the microspheres of the batch, which allows for quantification of the microsphere PSD as well as the evaluation of microstructure similarity as described in this paper. The overall time for XRM imaging depending on the specific instrument and desired resolution will take anywhere from 15 min to a few hours. The time required for AI analysis and quantification, while similarly dependent on the size of the imaging data, can be accelerated *via* parallel computing and automation. This means that within the span of several hours, the batch quality can be assessed *via* the XRM workflow. The FIB-SEM workflow (right side of Fig. 9) can be conducted in parallel to the XRM imaging as implied by Fig. 9 or can be conducted after the XRM determined batch assessment. The FIB-SEM imaging data is subjected to AI image analysis and segmentation as in the XRM workflow, though the overall time is a few times longer than the XRM images, due to both longer data acquisition and more challenging imaging process. From the FIB-SEM data, the microstructure CQAs such as the phase fractions and size distributions of API particles can be computed. Additionally, the pore sizes and intra-sphere spatial distributions can be quantified, which enable the imaging data to be used to simulate drug release. The FIB-SEM workflow has been established as a means of quantifying the precise intra-sphere microstructure of microsphere products [14]. The XRM workflow on the other hand, is able to establish the overall similarity in microstructure of a microsphere formulation (both intra-batch and inter-batch), addressing the question of the representativeness of the FIB-SEM imaged microsphere for the whole batch. While XRM allows for rapid characterization, the slower, destructive FIB-SEM workflow allows for in-depth quantification of the microstructure on selected representative microspheres from the samples. This correlative workflow offers the ability to quantify the microstructure CQAs (through FIB-SEM) and the intra- and inter-batch similarity (through XRM) and predict release *via* the extracted CQA and uniformity matrix.

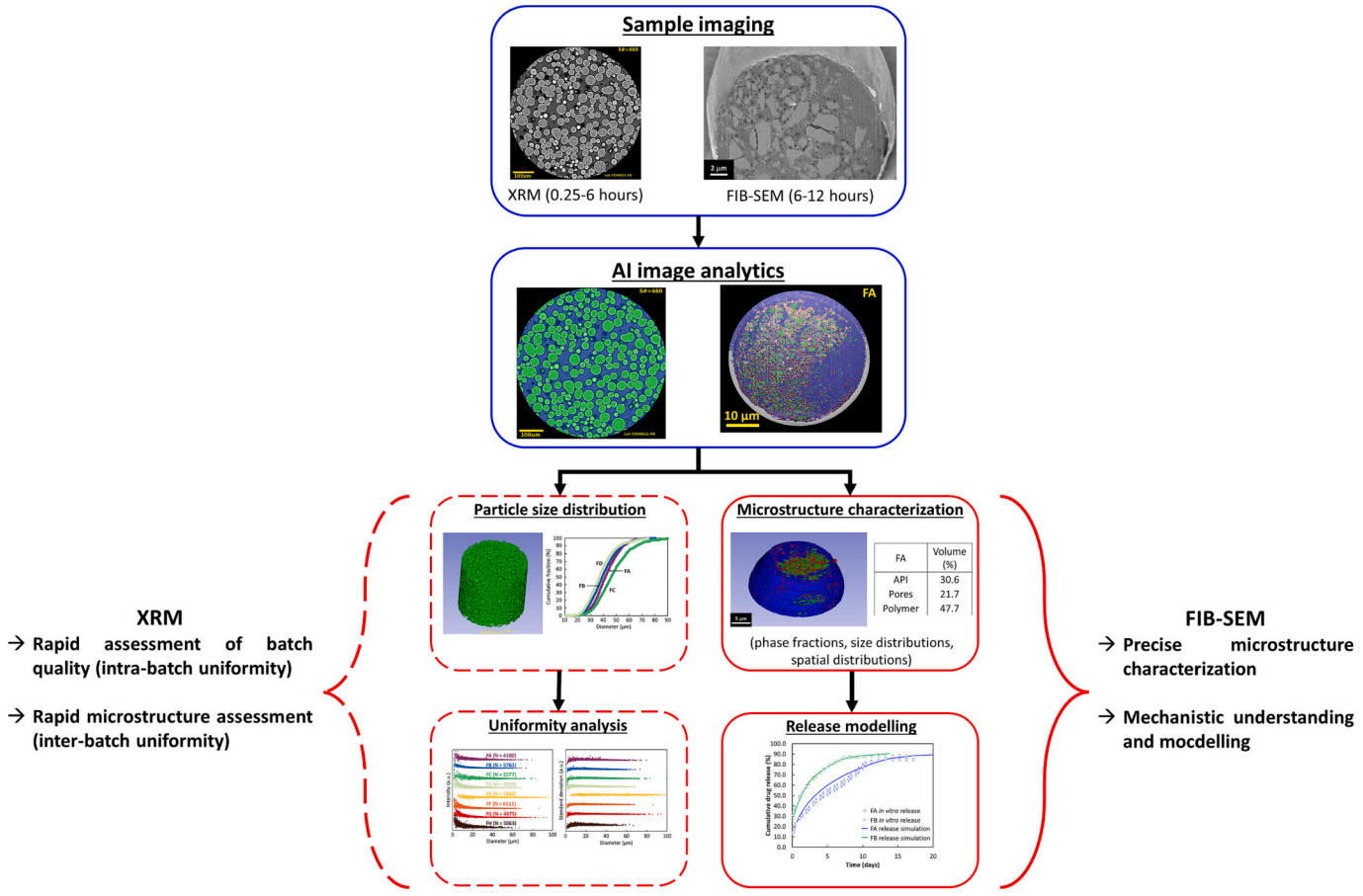

Fig. 9. Full correlative XRM and FIB-SEM workflow, with XRM uniformity assessments indicated and FIB-SEM microstructure CQA characterization indicated.

Correlating precise microstructure CQAs extracted from FIB-SEM with XRM analysis provides an efficient assessment of formulation and process parameters, eliminating, or reducing extensive FIB-SEM on large numbers of samples. Once the XRM signal intensity and intensity variation is correlated to the underlying microstructure determined by FIB-SEM, XRM can then be used as a rapid tool in identifying ideal formulation and process parameters. Further, the size distribution calculated from XRM can be combined with the FIB-SEM based release prediction to understand how particle size dictates the duration and kinetics of drug release. The potential for XRM as a rapid microstructure quality control tool can greatly aid in cost-effective characterization of new and existing drug products with high throughput.

This correlative workflow also provides a potential path to establishing microstructure similarity at both intra-sphere (FIB-SEM) and inter-batch (XRM) scales, which is helpful to explore *in vitro* bioequivalence approaches.

4. Conclusions

X-ray microscopy (XRM) as a tool for assessing the intra-batch and inter-batch structural similarity of controlled release microsphere drug products has been demonstrated *via* analysis of x-ray intensity and its intra-microsphere variation. The particle size distribution determined by XRM imaging was similar to that determined by AccuSizer while XRM mitigates the impact of particle aggregation. Analysis of the XRM signal intensity showed that all eight formulations prepared using different manufacturing parameters had similar microstructure for microspheres with diameters of 20 µm or above. This observation quantitatively confirms the overall intra-batch similarity of microstructure in the microspheres intra-batch. In addition, the inter-batch similarity in microstructure assessed using variations in the XRM signal intensity was shown to be related to the microsphere internal structure and was successfully correlated to the manufacturing parameters and release performance as a gap-bridging quality attribute.

CRediT authorship contribution statement

Andrew G. Clark: Formal analysis, Investigation, Visualization, Writing – original draft, Writing – review & editing. **Ruifeng Wang:** Formal analysis, Investigation, Visualization, Writing – review & editing. **Josh Lomeo:** Investigation, Visualization, Writing – review & editing. **Yan Wang:** Supervision, Visualization, Writing – review & editing. **Aiden Zhu:** Formal analysis, Software, Visualization. **Mike Shen:** Formal analysis, Software. **Quanying Bao:** Investigation, Writing – review & editing. **Diane J. Burgess:** Conceptualization, Funding acquisition, Project administration, Supervision, Writing – review & editing. **Bin Qin:** Investigation, Supervision, Writing – review & editing. **Shawn Zhang:** Conceptualization, Funding acquisition, Project administration, Resources, Supervision, Writing – review & editing.

Data availability

Data will be made available on request.

Acknowledgments

This work was partially supported by the Broad Agency Announcement (BAA) Contract # 75F40119C10157 from the U.S. Food and Drug Administration (FDA). The content is solely the responsibility of the authors and does not necessarily represent the official views or policies

of the U.S. FDA.

Appendix A. Supplementary data

Supplementary data to this article can be found online at https://doi.org/10.1016/j.jconrel.2023.05.019.

References

[1] T. Casalini, A. Cingolani, E. Scibona, Modeling the microenvironment-dependent degradation of drug-loaded polylactic- co-glycolic microparticles, Ind. Eng. Chem. Res. 60 (2021) 10683–10698, https://doi.org/10.1021/acs.iecr.1c01013.

[2] L.L. Lao, S.S. Venkatraman, N.A. Peppas, Modeling of drug release from biodegradable polymer blends, Eur. J. Pharm. Biopharm. 70 (2008) 796–803, https://doi.org/10.1016/j.ejpb.2008.05.024.

[3] K.G. Janoria, A.K. Mitra, Effect of lactide/glycolide ratio on the in vitro release of ganciclovir and its lipophilic prodrug (GCV-monobutyrate) from PLGA microspheres, Int. J. Pharm. 338 (2007) 133–141, https://doi.org/10.1016/j.ijpharm.2007.01.038.

[4] S. Fredenberg, M. Wahlgren, M. Reslow, A. Axelsson, The mechanisms of drug release in poly(lactic-co-glycolic acid)-based drug delivery systems - A review, Int. J. Pharm. 415 (2011) 34–52, https://doi.org/10.1016/j.ijpharm.2011.05.049.

[5] W. Jiang, R.K. Gupta, M.C. Deshpande, S.P. Schwendeman, Biodegradable poly (lactic-co-glycolic acid) microparticles for injectable delivery of vaccine antigens, Adv. Drug Deliv. Rev. 57 (2005) 391–410, https://doi.org/10.1016/j.addr.2004.09.003.

[6] K. Park, S. Skidmore, J. Hadar, J. Garner, H. Park, A. Otte, B.K. Soh, G. Yoon, D. Yu, Y. Yun, Injectable, long-acting PLGA formulations: Analyzing PLGA and understanding microparticle formation, J. Control. Release. 304 (2019) 125–134.

[7] N.K. Varde, D.W. Pack, Microspheres for controlled release drug delivery, Expert Opin. Biol. Ther. 4 (2004) 35–51.

[8] H. Zhong, G. Chan, Y. Hu, H. Hu, D. Ouyang, A comprehensive map of FDA-approved pharmaceutical products, Pharmaceutics. 10 (2018) 263.

[9] Y. Wang, D.J. Burgess, Microsphere technologies, in: Long Act. Inject. Implant, Springer, 2012, pp. 167–194.

[10] Y. Wang, Q. Wen, S. Choi, FDA's regulatory science program for generic PLA/PLGA-based drug products, Am Pharm Rev. 19 (2016) 5–9.

[11] R.-K. Chang, A. Raw, R. Lionberger, L. Yu, Generic development of topical dermatologic products: formulation development, process development, and testing of topical dermatologic products, AAPS J. 15 (2013) 41–52.

[12] S. Zhang, D. Wu, L. Zhou, Characterization of controlled release microspheres using FIB-SEM and image-based release prediction, AAPS PharmSciTech. 21 (2020), https://doi.org/10.1208/s12249-020-01741-w.

[13] S. Zhang, G. Byrne, Characterization of transport mechanisms for controlled release polymer membranes using focused ion beam scanning electron microscopy image-based modelling, J. Drug Deliv. Sci. Technol. 61 (2021), 102136, https://doi.org/10.1016/j.jddst.2020.102136.

[14] A.G. Clark, R. Wang, Y. Qin, Y. Wang, A. Zhu, J. Lomeo, Q. Bao, D.J. Burgess, J. Chen, B. Qin, Assessing microstructural critical quality attributes in PLGA microspheres by FIB-SEM analytics, J. Control. Release. 349 (2022) 580–591.

[15] S. Zhang, K. Nagapudi, M. Shen, J. Lomeo, Y. Qin, A. Zhu, P. Nayak, D. Chang, R. N. Hannoush, Release mechanisms and practical percolation threshold for long-acting biodegradable implants: An image to simulation study, J. Pharm. Sci. 111 (2021) 1896–1910.

[16] J.F. Gamble, M. Tobyn, S. Zhang, A. Zhu, J. Šalplachta, J. Matula, T. Zikmund, J. Kaiser, P. Oberta, Characterization of the morphological nature of hollow spray dried dispersion particles using X-ray submicron-computed tomography, AAPS PharmSciTech. 23 (2022) 1–7.

[17] K. Nagapudi, A. Zhu, D.P. Chang, J. Lomeo, K. Rajagopal, R.N. Hannoush, S. Zhang, Microstructure, quality, and release performance characterization of long-acting polymer implant formulations with X-ray microscopy and quantitative AI analytics, J. Pharm. Sci. (2021), https://doi.org/10.1016/j.xphs.2021.05.016.

[18] S. Zhang, P.A. Stroud, A. Zhu, M.J. Johnson, J. Lomeo, C.L. Burcham, J. Hinds, K. A.-F. Blakely, M.J. Walworth, Characterizing the impact of spray dried particle morphology on tablet dissolution using quantitative X-ray microscopy, Eur. J. Pharm. Sci. 165 (2021), 105921.

[19] E. Yost, P. Chalus, S. Zhang, S. Peter, A.S. Narang, Quantitative X-ray microcomputed tomography assessment of internal tablet defects, J. Pharm. Sci. 108 (2019) 1818–1830.

[20] R. Wang, Q. Bao, A.G. Clark, Y. Wang, S. Zhang, D.J. Burgess, Characterization and in vitro release of minocycline hydrochloride microspheres prepared via coacervation, Int. J. Pharm. 628 (2022), 122292, https://doi.org/10.1016/j.ijpharm.2022.122292.

[21] J.V. Andhariya, S. Choi, Y. Wang, Y. Zou, D.J. Burgess, J. Shen, Accelerated in vitro release testing method for naltrexone loaded PLGA microspheres, Int. J. Pharm. 520 (2017) 79–85.

[22] S. Zhang, J. Neilly, A. Zhu, J. Chen, G. Danzer, Quantitative characterization of crystallization in amorphous solid dispersion drug tablets using x-ray micro-computed tomography, Microsc. Microanal. 24 (2018) 1400–1401.

[23] H. Xi, A. Zhu, G.R. Klinzing, L. Zhou, S. Zhang, A.J. Gmitter, K. Ploeger, P. Sundararajan, M. Mahjour, W. Xu, Characterization of spray dried particles through microstructural imaging, J. Pharm. Sci. 109 (2020) 3404–3412.

[24] S. Zhang, A.P. Byrnes, J. Jankovic, J. Neilly, Management, analysis, and simulation of micrographs with cloud computing, Micros. Today. 27 (2019) 26–33.

[25] D. Kalasová, T. Zikmund, L. Pína, Y. Takeda, M. Horváth, K. Omote, J. Kaiser, Characterization of a laboratory-based X-ray computed nanotomography system for propagation-based method of phase contrast imaging, IEEE Trans. Instrum. Meas. 69 (2020) 1170–1178, https://doi.org/10.1109/TIM.2019.2910338.

[26] H. Li, J. Li, J. Bodycomb, G.S. Patience, Experimental methods in chemical engineering: Particle size distribution by laser diffraction—PSD, Can. J. Chem. Eng. 97 (2019) 1974–1981.

[27] C.E. Cann, Quantitative CT for determination of bone mineral density: a review, Radiology. 166 (1988) 509–522.

[28] W. Huda, R.M. Slone, Review of radiologic physics, Lippincott Williams & Wilkins, 2003.

[29] A.G. Clark, Method for density measurement of materials using computed tomography with diffraction artifact correction, in: US Application No.: 63/367,532, 2022.

[30] J. Siepmann, F. Siepmann, Mathematical modeling of drug delivery, Int. J. Pharm. 364 (2008) 328–343, https://doi.org/10.1016/j.ijpharm.2008.09.004.

[31] Y. Fu, W.J. Kao, Drug release kinetics and transport mechanisms of non-degradable and degradable polymeric delivery systems, Expert Opin. Drug Deliv. 7 (2010) 429–444, https://doi.org/10.1517/17425241003602259.